

# Tumor-Targeting, MicroRNA-Silencing Porous Silicon Nanoparticles for Ovarian Cancer Therapy

Alessandro Bertucci,<sup>†,‡,§,¶</sup> Kang-Hoon Kim,<sup>#,¶</sup> Jinyoung Kang,<sup>‡</sup> Jonathan M. Zuidema,<sup>†</sup> Seo Hyeon Lee,<sup>△</sup> Ester J. Kwon,<sup>§</sup> Dokkyoung Kim,<sup>○</sup> Stephen B. Howell,<sup>||</sup> Francesco Ricci,<sup>‡,¶</sup> Erkki Ruoslahti,<sup>¶</sup> Hyeung-Jin Jang,<sup>\*,‡,¶</sup> and Michael J. Sailor<sup>\*,†,‡,§,||,¶</sup>

<sup>†</sup>Department of Chemistry and Biochemistry, <sup>‡</sup>Department of Nanoengineering, <sup>§</sup>Department of Bioengineering, and <sup>||</sup>Moores Cancer Center, University of California, San Diego, La Jolla, California 92093, United States

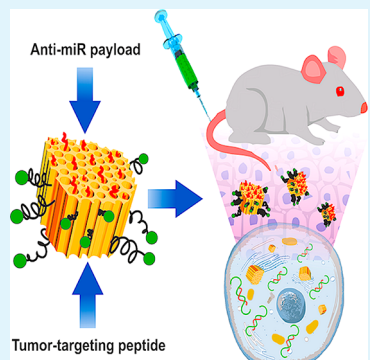
<sup>‡</sup>Department of Chemical Sciences and Technologies, University of Rome Tor Vergata, Rome, 00133, Italy

<sup>#</sup>Department of Science in Korean Medicine, <sup>△</sup>Department of Biomedical Science, Graduate School, <sup>○</sup>Department of Anatomy and Neurobiology, College of Medicine, and <sup>◆</sup>Department of Biochemistry, College of Korean Medicine, Kyung Hee University, Seoul, 02447, Republic of Korea

<sup>\*</sup>Cancer Center, Sanford Burnham Prebys Medical Discovery Institute, La Jolla, California 92037, United States

## Supporting Information

**ABSTRACT:** Silencing of aberrantly expressed microRNAs (miRNAs or miRs) has emerged as one of the strategies for molecular targeted cancer therapeutics. In particular, miR-21 is an oncogenic miRNA overexpressed in many tumors, including ovarian cancer. To achieve efficient administration of anti-miR therapeutics, delivery systems are needed that can ensure local accumulation in the tumor environment, low systemic toxicity, and reduced adverse side effects. In order to develop an improved anti-miR therapeutic agent for the treatment of ovarian cancer, a nanoformulation is engineered that leverages biodegradable porous silicon nanoparticles (pSiNPs) encapsulating an anti-miR-21 locked nucleic acid payload and displaying a tumor-homing peptide for targeted distribution. Targeting efficacy, miR-21 silencing, and anticancer activity are optimized in vitro on a panel of ovarian cancer cell lines, and a formulation of anti-miR-21 in a pSiNP displaying the targeting peptide CGKRK is identified for in vivo evaluation. When this nanoparticulate agent is delivered to mice bearing tumor xenografts, a substantial inhibition of tumor growth is achieved through silencing of miR-21. This study presents the first successful application of tumor-targeted anti-miR porous silicon nanoparticles for the treatment of ovarian cancer in a mouse xenograft model.



**KEYWORDS:** peptide targeting, nanomedicine, miR-21, cancer therapy, microRNA silencing, *in vivo*, locked nucleic acid, COV-318 ovarian cancer xenograft

## INTRODUCTION

Ovarian cancer is the most lethal gynecologic malignancy and one of the leading causes of cancer mortality among women.<sup>1,2</sup> Despite a high initial response rate to surgery and chemotherapy, the majority of advanced-stage patients develop recurrent cancer and eventually succumb to drug-resistant disease.<sup>3</sup> The search for innovative and alternative therapies has revealed aberrantly expressed microRNAs (miRNAs or miRs) as potential molecular targets.<sup>4–6</sup> miRNAs are short endogenous noncoding RNAs that regulate gene expression at the post-transcriptional level by either repressing translation or inducing degradation of the target RNA transcript. Thus, they play a pivotal role in the regulation of major cellular processes, including cell metabolism, differentiation, proliferation, and apoptosis.<sup>7</sup> There is established evidence that dysregulation and aberrant expression of certain miRNAs, called oncomiRs, is associated with both early development and advanced stages of cancer.<sup>8,9</sup> Anti-miR therapy is an anticancer strategy that uses antisense oligonucleotides to silence these upregulated

oncomiRs.<sup>10–13</sup> The repression of a specific oncomiR can induce a cascade of additional beneficial effects, as a single miRNA can simultaneously target different messenger RNAs (mRNAs) and regulate multiple biological pathways.<sup>7,14</sup>

As robust correlations between miRNA signature and cancer development have become more established,<sup>4–6</sup> several anti-miR therapies have been deployed against various animal cancer models, including breast, lung, and lymphoma.<sup>12,15,16</sup> Of particular relevance to the present work, systemic administration of anti-miR therapeutics has been demonstrated to reduce tumor burden in mice bearing ovarian cancer xenografts.<sup>17</sup> This prior study delivered the anti-miR as a free entity, using no delivery vehicle. While the *in vivo* stability of anti-miR agents has been achieved by employing chemically modified nucleic acid structures or non-natural oligonucleo-

Received: May 7, 2019

Accepted: June 17, 2019

Published: June 17, 2019



ACS Publications

© 2019 American Chemical Society

23926

DOI: 10.1021/acsami.9b07980

ACS Appl. Mater. Interfaces 2019, 11, 23926–23937

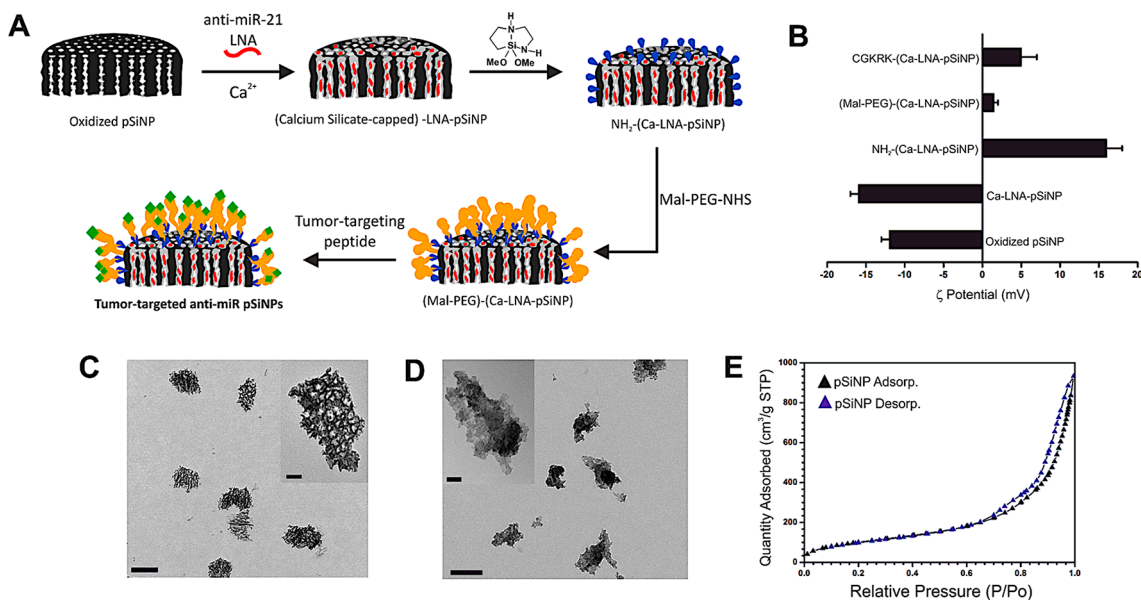


**Figure 1.** Preparation of tumor-targeted anti-miR porous silicon nanoparticles (pSiNPs). (A) Schematic illustration of the procedure followed to load the particles with anti-miR LNA oligonucleotides and then attach the PEG and tumor-targeting peptide groups. (B)  $\zeta$ -Potential measurements at each step of functionalization. (C) Transmission electron microscope (TEM) image of unmodified pSiNPs (scale bar = 200 nm); the inset shows a closer view of a single nanoparticle (scale bar = 50 nm). (D) TEM image of calcium silicate-capped LNA pSiNPs (scale bar = 200 nm); the inset shows a closer view of a single nanoparticle (scale bar = 50 nm). (E) Cryogenic nitrogen adsorption–desorption isotherm of the empty, unmodified pSiNPs.

tides,<sup>12,18,19</sup> there is a need for delivery vehicles to efficiently transport anti-miR therapeutics to the target tumor in order to improve bioavailability, lower systemic toxicity, and reduce the off-target effects of these therapeutics.<sup>20</sup>

Several soft nanoparticle systems encapsulating anti-miR oligonucleotides have been proposed for anticancer therapy, including liposome-<sup>21–23</sup> and polymer-based formulations.<sup>16,24,25</sup> Peptide-based constructs have been reported that target the tumor microenvironment and facilitate cell penetration, allowing for efficient anti-miR therapy *in vivo*.<sup>15</sup> Inorganic nanocarriers have also been studied for the delivery of anti-miR therapeutics, including gold<sup>26,27</sup> and mesoporous silica nanoparticles.<sup>28–30</sup> While less studied than the above, porous silicon nanoparticles (pSiNPs)<sup>31–33</sup> have recently emerged as candidate delivery vehicles for nucleic acid therapeutics due to their safe *in vivo* degradation pathway and their large capacity for nucleic acid-based therapeutics.<sup>34</sup> The clinical application of pSiNPs is still at a very early stage. While some formulations have recently been tested in clinical trials,<sup>31</sup> chemical and medical challenges remain.

With regard to cancer therapy, there have been several reports of pSiNPs carrying RNA-based payloads for gene silencing. These studies used small, interfering RNA (siRNA) payloads to silence target mRNA (mRNA), the therapeutic approach known as RNA interference (RNAi).<sup>35</sup> However, the use of pSiNPs to load and deliver a microRNA-silencing payload for anti-miR cancer treatment has not been investigated. The successful treatment of cancer *in vivo* by administration of a single anti-miR oligonucleotide in a tumor-targeted manner has been a recent breakthrough,<sup>15</sup> and it provides strong motivation to explore anti-miR payloads. To date there is one example of pSiNPs used for miR inhibition; this is based on porous silicon–polymer nanocomposites for the delivery of a peptide nucleic acid (PNA) targeting miR-122, a microRNA involved in cholesterol biosynthesis in the

liver.<sup>36</sup> This study established biocompatibility and miRNA inhibition *in vivo*, although no therapeutic outcome was demonstrated. Here, we show for the first time that pSiNPs can be used to leverage microRNA silencing as an effective anticancer therapeutic. The present study is the first to combine the tumor-targeting capabilities of peptide-modified pSiNPs with an anti-miR payload to target and treat tumors *in vivo*.

## RESULTS AND DISCUSSION

For this report we focused on miR-21, which is a commonly upregulated oncomiR across a number of cancers.<sup>37–39</sup> Silencing of miR-21 has been demonstrated to provide an anticancer effect in animal models of pancreatic, breast, and lung cancers and glioblastoma when the anti-miR oligonucleotides were delivered by means of vectors composed of polymer, lipid, or RNA nanoconstructs.<sup>16,40–42</sup> miR-21 is overexpressed in ovarian carcinomas compared to healthy tissues, and it is associated with abnormal cell proliferation, acquired multidrug resistance, and tumor invasion.<sup>4,43,44</sup> However, anti-miR-21 therapeutic strategies have not been investigated yet *in vivo* in ovarian cancer models. In this context, a pSiNP provides an attractive delivery platform because of the tunable pore sizes that can efficiently accommodate desired payloads, the versatile surface chemistry that facilitates custom functionalization, and the biocompatible degradation pathway with end products excreted from the body through the urine.<sup>31,34</sup>

We employed a locked nucleic acid (LNA) against microRNA 21 (miR-21) as the therapeutic payload. LNAs are among the most advanced tools for microRNA silencing, as they hybridize with their target with exceptional affinity and specificity and their artificial backbone imparts high resistance to nucleolytic degradation.<sup>12,45,46</sup> High *in vivo* stability is very important for this type of therapeutic; indeed, the only miRNA therapeutic currently in phase II clinical trials is an LNA:

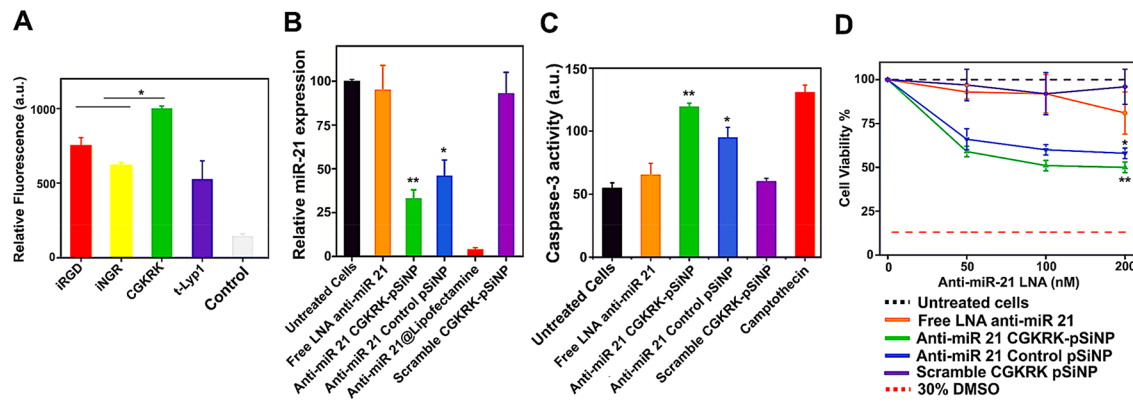


**Figure 2.** Investigation of cellular targeting, microRNA silencing, and cellular toxicity of anti-miR-21 pSiNPs in a model OAW42 ovarian cancer cell line. (A) Flow cytometry data evaluating the efficiency of the peptide targeting group to localize pSiNPs to OAW42 cells, quantified as relative fluorescence intensity from the FAM-labeled peptides attached to pSiNPs and associated with OAW42 cell populations (mean value  $\pm$  SD,  $n = 3$ ,  $*p < 0.05$ ). (B) Relative miR-21 expression, evaluated by reverse transcription quantitative polymerase chain reaction (RT-qPCR), in OAW42 cells treated with the indicated nanoparticle formulations (mean value  $\pm$  SD,  $n = 6$ ,  $*p < 0.05$ ,  $**p < 0.01$ ). (C) Caspase-3 assay showing the increase in intensity of fluorescence from the activity marker upon induction of apoptosis in OAW42 cells treated with the indicated nanoparticle formulations (mean value  $\pm$  SD,  $n = 6$ ,  $*p < 0.05$ ,  $**p < 0.01$ ). (D) Viability (MTT assay) of OAW42 cells incubated with the indicated nanoparticle formulations at multiple concentrations of the indicated LNA (50 nM, 100 nM, 200 nM) (mean value  $\pm$  SD,  $n = 6$ ,  $*p < 0.05$ ,  $**p < 0.01$ ).

“miravirsen”, an inhibitor of miR-122 developed by Santaris Pharma/Roche.<sup>13,47</sup> The pSiNPs were loaded with the LNA therapeutic following the procedure shown in Figure 1A. The detailed synthetic procedure is provided in the Methods section. First, pSiNPs<sup>48</sup> of average diameter  $182 \pm 6$  nm [by dynamic light scattering (DLS) (Figure S1, Supporting Information, SI)] and transmission electron microscopy (TEM) (Figure 1)], porosity  $46 \pm 1\%$ ,<sup>49</sup> pore volume  $1.29 \text{ cm}^3 \text{ g}^{-1}$ , and average pore size  $14.2 \text{ nm}$  (calculated from nitrogen adsorption–desorption isotherms using the Brunauer–Emmett–Teller or BET method, Figure 1E) were loaded with the anti-miR-21 LNA payload following a calcium silicate trapping procedure.<sup>34b</sup> This involved stirring the pSiNPs in an ethanol/water solution containing the LNA oligonucleotides in the presence of a high concentration (2 M) of calcium chloride ( $\text{CaCl}_2$ ). Oligonucleotide loading was quantified by means of UV-vis spectroscopy using Quasar 570-labeled oligonucleotides to be  $\sim 17\%$  by mass (defined in terms of the mass of the nucleic acid divided by the total mass of nanoparticle + nucleic acid), corresponding to  $\sim 28$  nmol of LNA/mg of porous silicon. This value is comparable to that reported by Beavers et al. for loading of a peptide nucleic acid (PNA)-based anti-miR oligonucleotide in pSiNPs.<sup>36</sup> In the present case, anti-miR loading was accomplished without use of a coadjuvant polymer for encapsulation of the payload. The calcium silicate trapping method produced a high encapsulation efficiency ( $97 \pm 2\%$ ,  $n = 6$ ), indicating that loss of nucleic acid was minimal with this loading protocol (see Methods section) and that slightly more hydrophobic macromolecules such as LNAs can be encapsulated as efficiently as native RNA strands.<sup>34b</sup> The process resulted in a slight increase in the hydrodynamic diameter of nanoparticles (Figure S1, SI) and a shift in the  $\zeta$ -potential to more negative values (from  $-12 \pm 1$  to  $-16 \pm 1$  mV, Figure 1B). The porous nanostructure in the calcium silicate-trapped, LNA-loaded pSiNPs (Ca-LNA-pSiNPs) was less apparent compared to unmodified pSiNPs (Figure 1C); the observed morphology in the TEM was consistent with partially or completely sealed pores (Figure 1D).

To confirm adequate trapping of the LNA payload, the calcium silicate-sealed nanoparticles were subjected to an in

vitro release protocol simulating physiological conditions (phosphate-buffered saline, PBS, pH 7.4, 37 °C). The particles dissolved and released the LNA payload with a temporal release profile similar to that described in our previous work using an siRNA payload.<sup>34b</sup> Nearly quantitative release of the oligonucleotide payload was observed within 24 h, and approximately 80% of release occurred during the first 8 h (Figure S2, SI).

The final nanoparticle construct contained an overcoating of polyethylene glycol (PEG) to improve circulation and one of a collection of targeting peptides for selective tissue homing. These were attached to the Ca-LNA-pSiNPs through the agency of a cyclic azasilane reagent (DMDASCO, 2,2-dimethoxy-1,6-diaza-2-silacyclooctane), which generated primary amine groups on the particle surface via a ring-opening click reaction.<sup>50</sup> The presence of the amine linkers was confirmed by  $\zeta$ -potential measurement, which showed a shift to positive values ( $+16 \pm 2$  mV) upon functionalization (Figure 1B), and by Fourier transform infrared (FTIR) spectroscopy (N–H stretching and bending modes, Figure S3, SI). This demonstrates that the above chemistry can be successfully performed on a silicon particle whose surface harbors a calcium silicate coating. The PEG chains were then grafted to the primary amines. A maleimide-PEG-succinimidyl valerate (MAL-PEG-SVA) was used, which formed amide bonds between the succinimidyl valerate and the surface amine groups, leaving a free maleimide group at the distal end. The measured  $\zeta$ -potential became less positive at this point ( $+1.5 \pm 0.5$  mV, Figure 1B), and FTIR spectroscopy confirmed the presence of the functional group (strong aliphatic C–H stretching and amide C=O stretching bands, Figure S3, SI). The candidate tumor-targeting peptide was then grafted to the nanoparticle via the maleimide, which formed a covalent thioether bond with a free-cysteine on the peptide (Figure 1A). The surface charge became slightly more positive at this point ( $\zeta$ -potential  $+5 \pm 2$  mV, Figure 1B), and the FTIR spectrum of the final construct confirmed the presence of the candidate peptide [broad N–H stretching above  $3000 \text{ cm}^{-1}$  and strong signals in the amide C=O region; Figure S3 (SI) shows the data for targeting peptide CGKRK, sequence Cys-Gly-Lys-Arg-

Lys]. The density of peptides grafted to the pSiNPs was determined using FAM-labeled peptides, by measurement of the optical absorbance of the supernatant ( $\lambda = 548$  nm), and was found to be  $39 \pm 6$  nmol peptide/mg pSiNPs ( $n = 15$ ). Accordingly, we estimate that the PEG surface coverage was at least 40 nmol PEG/mg pSi, which translates into  $\geq 14\%$  by mass.

Cellular targeting, miRNA silencing, and therapeutic properties of the nanoparticles were then screened *in vitro* using the OAW42 human ovarian cancer cell line as a preliminary model. We prepared a small library of anti-miR pSiNPs functionalized with different tumor-targeting peptides and sought to identify the formulation providing the highest nanoparticle accumulation in the cells. Peptides are appealing targeting elements because they have a relatively small size, they typically do not induce an immunogenic response, their synthesis and chemical modification procedures are well established, and the presentation of multiple copies of a peptide on a single nanoparticle can significantly increase avidity for the target.<sup>51,52</sup> Prior work has established that pSiNPs can be quite selectively targeted to specific tissues using peptide-based ligands.<sup>53–56</sup> The following peptides were screened: iRGD, iNGR, CGKRK, and truncated LyP-1 (t-LyP-1) (all peptide sequences are reported in the **Methods** section). Each of the above peptides has been demonstrated to display tumor-homing and tumor-penetrating properties previously, though they engage different targeting pathways.<sup>57</sup> However, none of these has been used as an active ligand mounted on pSiNPs for targeting ovarian cancer. For comparison, we included in the study a control peptide, CREK, a variant of a peptide displaying no targeting activity in cell cultures.<sup>58</sup> Following the conjugation procedure described above, FAM-labeled peptides (FAM is the fluorescent label 5-carboxyfluorescein) were coupled to the PEGylated, anti-miR-loaded pSiNPs. OAW42 cells were incubated with the different peptide-pSiNP formulations and binding was quantified by flow cytometry (Figure 2A). The CGKRK-pSiNPs showed the highest nanoparticle accumulation. Confocal microscopy of OAW42 cells incubated with CGKRK-pSiNPs loaded with a Quasar 570-labeled oligonucleotide confirmed substantial intracellular localization of both the FAM-labeled CGKRK and the oligonucleotide payload after 4 and 24 h (Figure S4, SI). The confocal micrographs were consistent with a nanoparticle cellular uptake and payload delivery involving an endocytic pathway,<sup>31,34,56</sup> although the present study did not systematically investigate the endosomal cell internalization and intracellular trafficking mechanism(s). On the basis of these results, we focused on the anti-miR-21 CGKRK-pSiNP construct for the next set of experiments.

Silencing of microRNA by the released LNA was evaluated by quantitative reverse transcription polymerase chain reaction (RT-qPCR) assay. Incubation of OAW42 cells with anti-miR-21 CGKRK-pSiNPs led to a significant reduction ( $\sim 70\%$ ) of the relative abundance of miR-21 compared to untreated cells (Figure 2B). CGKRK-pSiNPs loaded with a scrambled LNA sequence were used to assess any nonspecific silencing effect; no difference was observed compared to control cells. Similarly, administration of free anti-miR-21 LNA without pSiNPs caused no silencing. We also ran a control experiment using the CREK control peptide in place of the CGKRK targeting peptide, on pSiNPs carrying anti-miR-21 LNA. The cationic CREK peptide was chosen because it displayed a substantially reduced level of cellular targeting *in vitro* (Figure

2A). Consistent with the lower targeting efficacy, anti-miR-21 CREK-pSiNPs displayed a lower ability to suppress miR-21 expression ( $\sim 55\%$ ) relative to the CGKRK-modified particles (Figure 2B). We note that the small difference in microRNA silencing observed between CREK-pSiNPs and CGKRK-pSiNPs is likely due to the long incubation time (48 h) used in the experiments, which increased the opportunity for non-targeted pSiNPs to become internalized.

We next investigated whether blocking of miR-21 induced downstream effects on cell apoptosis and viability. Caspase-3 is an early apoptotic cell marker and monitoring its activation can be used to assess induction of apoptosis. We found that OAW42 cells treated with anti-miR-21 CGKRK-pSiNPs showed the highest caspase-3 activity, i.e., fluorescence emission triggered by the enzymatic activity of caspase-3 on a fluorogenic substrate. The level of caspase-3 activity was comparable to the level observed from cells treated with camptothecin, a pro-apoptotic drug commonly used as a positive control in caspase assays.<sup>59</sup> In contrast, free anti-miR-21 LNA and CGKRK-pSiNPs loaded with a scrambled LNA did not result in any significant increase in caspase-3 activity relative to untreated cells (Figure 2C). Treatment of OAW42 cells with anti-miR-21 CGKRK-pSiNPs led to a significant decrease in cell viability ( $\sim 50\%$ ), which demonstrated the potential efficacy of the anti-miR strategy in generating a therapeutic effect (Figure 2D). Dosing was varied from 0 to 200 nM LNA, and toxicity from the anti-miR-21 CGKRK-pSiNPs became apparent for LNA concentrations  $\geq 50$  nM. By contrast, cellular toxicity from the free anti-miR-21 LNA (not loaded into a nanoparticle) was detected only at the highest concentration studied (200 nM). We observed no adverse effect on viability when a scrambled LNA CGKRK-pSiNP formulation corresponding to 200 nM LNA concentration was used. Thus, the nanocarrier system itself (absent an active anti-miR payload) showed no cytotoxicity over the concentration range studied. Treatment of the OAW42 cells with control pSiNPs loaded with anti-miR-21 LNA (LNA concentration 200 nM) caused a decrease in cell viability of 42%. The lower potency compared to the targeted construct (anti-miR-21 CGKRK-pSiNPs) is consistent with the trends observed in the RT-qPCR and caspase activity assay data (Figure 2B–D). Motivated by the effectiveness of anti-miR-21 CGKRK-pSiNPs in the ovarian cancer cell line OAW42, we next sought to evaluate anti-miR pSiNPs across a representative pool of ovarian cancer cells. The goals were 2-fold: (1) to identify the most effective targeting peptide and (2) to establish the response rate to anti-miR pSiNPs across a panel of human ovarian cancer cells, in order to select an optimal nanoparticle formulation and tumor model for an *in vivo* study. We evaluated targeting efficacy and cytotoxic activity on six additional ovarian cancer cell lines (CAOV-3, COV-318, OVCAR-8, Kuramochi, KF-28, IGROV-1). To identify the optimal targeting peptide, each cell line was exposed to the selection of targeting-peptide-functionalized pSiNPs described above, and nanoparticle accumulation in the cells was analyzed by means of flow cytometry (fluorescence signal from the FAM-labeled peptides). Figure 3A summarizes the results obtained across the different cell lines (OAW42 cells were also included for completeness). We found that CGKRK- and iRGD-pSiNPs showed the highest accumulation, as measured by flow cytometry, generating the most intense fluorescence signals in five out of six cell lines [Figures 3A and S5 (SI)]. Only Kuramochi cells showed a statistically significant

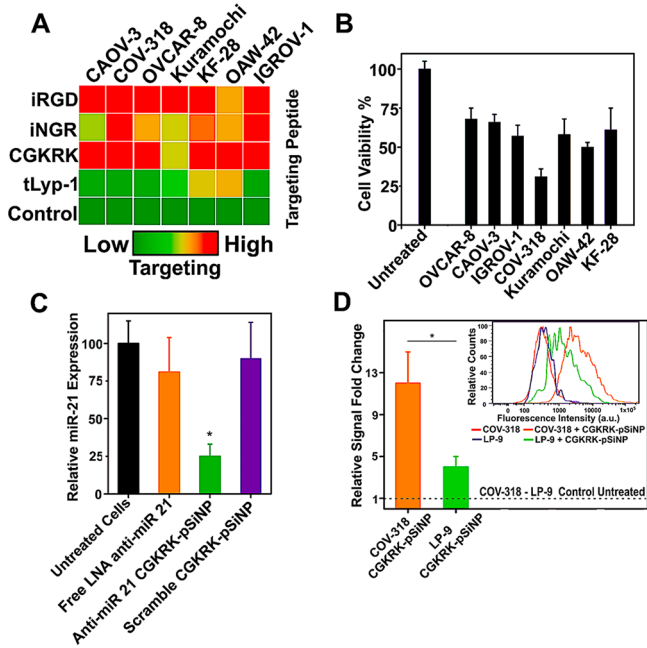


**Figure 3.** Screens of targeting efficacy and anticancer activity for anti-miR-21 pSiNPs using a collection of cell types and targeting peptides and response of the selected COV-318 cell line to anti-miR-21 pSiNPs containing the selected CGKRK targeting peptide. (A) An array of ovarian cancer cell lines (CAOV-3, COV-318, OVCAR-8, Kuramochi, KF-28, IGROV-1, OAW42) was incubated with pSiNPs functionalized with different FAM-labeled peptides, and the fluorescence intensity associated with the nanoparticle accumulation was measured by means of flow cytometry. The tumor-homing peptides were ranked on the basis of their relative cell-associated fluorescence signal as a measure of their targeting efficiency. CGKRK and iRGD gave the strongest signals. (B) Viability (MTT assay) of the different cell lines incubated with anti-miR-21 CGKRK-pSiNPs (LNA concentration 200 nM). The strongest reduction in viability was obtained for COV-318 cells. (C) RT-qPCR of miR-21 in COV-318 cells treated with the indicated nanoparticle formulations (mean value  $\pm$  SD,  $n = 6$ ,  $*p < 0.05$ ). (D) Relative fold change in fluorescence signal as measured by flow cytometry for COV-318 and LP-9 cells incubated with FAM-labeled CGKRK-pSiNPs, showing stronger accumulation (4-fold change) in COV-318 cells (mean value  $\pm$  SD,  $n = 3$ ,  $*p < 0.05$ ). The inset shows representative flow cytometry profiles for the indicated formulations.

preference for iRGD-pSiNPs (Figure S5, SIn). Conversely, CGKRK-pSiNPs gave statistically greater accumulation in OAW42 cells, as described above (Figure 2A). On the basis of the promising miR-21 silencing results obtained in OAW42 cells, we chose to focus on anti-miR pSiNPs decorated with the tumor-homing peptide CGKRK.

We next investigated the effect of the anti-miR-21 CGKRK-pSiNPs on the viability of the different ovarian cancer cell lines from the above screen. The majority of cell lines treated with anti-miR-21 CGKRK-pSiNPs (LNA concentration was 200 nM) showed a decrease of viability in the range of 30–50%. Among the cell lines studied, COV-318 cells were the most susceptible to the treatment, as their viability was reduced by more than 65% (Figure 3B). In order to confirm that the decrease in cell viability correlated with lower miR-21 expression, we performed RT-qPCR on the treated cells. The anti-miR-21 CGKRK-pSiNP treatment reduced expression of miR-21 by about 75%, indicating that the pSiNPs promoted silencing of the target miRNA, and this effect was correlated

with the observed reduction in cell viability (Figure 3C). Treatment with free anti-miR-21 LNA again caused no statistically significant silencing of the target miR-21. Furthermore, the use of CGKRK-pSiNPs loaded with a scrambled LNA showed no nonspecific miR-21 knockdown, as no difference was observed in this control compared to untreated cells (Figure 3C). We evaluated the specificity of tumor cell targeting relative to healthy cells by comparing the uptake of FAM-labeled CGKRK-pSiNPs into COV-318 cancer cells to the uptake in normal human peritoneal mesothelial LP-9 cells. As quantified by the intensity of the FAM signal, CGKRK-pSiNPs were taken up by COV-318 cells 4 times more efficiently than by LP-9 cells (Figure 3D). This agrees with the known ability of the CGKRK peptide to accumulate in tumor cells through its binding to the p32 protein, a mitochondrial protein in normal cells that is aberrantly expressed at the cell surface in many tumor cells.<sup>60</sup> Overexpression of p32 in ovarian cancer has been established in vitro, in vivo, and in human patients.<sup>61</sup>

With the optimal cell line (COV-318) and targeting peptide (CGKRK) identified, we next evaluated the in vivo performance of the anti-miR pSiNPs using COV-318 xenograft tumors subcutaneously transplanted into nude mice. We first evaluated the nanoparticle biodistribution in tumor-bearing mice. The experimental setup consisted of tumor-bearing mice intravenously injected with one of the following: (i) saline as negative control, (ii) pSiNPs functionalized with a control CRA (Cys-Arg-Ala) peptide, and (iii) tumor-targeting CGKRK-pSiNPs. The cationic CRA peptide was chosen as a control peptide for these in vivo studies, because it was thought that its short sequence would be less likely to contain any potential targeting motifs for the in vivo environment. Nonfunctionalized pSiNPs and PEGylated pSiNPs lacking a conjugated peptide were both previously shown not to provide organ-specific accumulation in mice compared to targeting peptide-modified pSiNPs.<sup>34,35</sup> In this work we chose to use more stringent control nanoparticles by incorporating a nontargeting peptide that carried a similar net positive charge as the CGKRK targeting peptide. This allowed the control nanoconstructs to display physicochemical features more similar to those of the investigated targeting pSiNPs, so that observed differences in in vivo behaviors (i.e., organ-specific accumulation) could be ascribed to the sequence-specific targeting capability of the CGKRK peptide with greater confidence. To simultaneously assess the stability of the nanosystem and track its individual components in vivo, biodistribution studies employing double-labeled nanoconstructs were performed, in which (1) the payload was a Quasar 670-labeled anti-miR-21 oligonucleotide and (2) the peptide attached to the outer surface of the particles was FAM-labeled. This allowed us to assess the integrity of the nanosystem in vivo by recording the fluorescence intensity of both the payload and the pSiNP-attached peptide in each harvested organ. Analysis of the red Quasar 670 fluorescence emission in harvested organs showed that a substantial amount of the oligonucleotide payload accumulated in the tumor in mice administered CGKRK-pSiNPs (Figure 4A). The fluorescence emission in tumors harvested from these mice ( $n = 6$ ) was 3 times more intense than in saline-injected control mice. Moreover, CGKRK-pSiNPs showed higher accumulation in the tumors compared to control CRA-pSiNPs (Figure 4A,B). Mice injected with control CRA-pSiNPs showed a more widespread distribution in the organs, with substantial

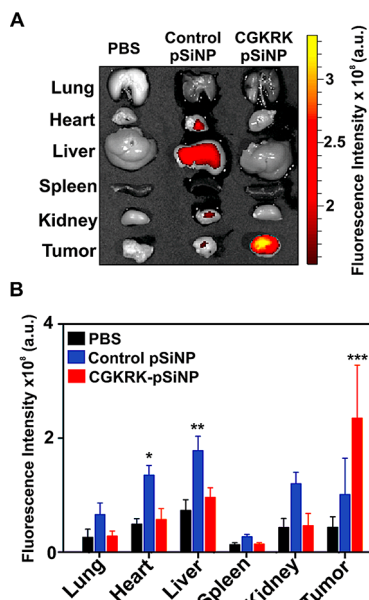


**Figure 4.** Biodistribution in nude mice bearing subcutaneous COV-318 xenograft tumors, comparing targeted and nontargeted nanoparticles by tracking the Quasar 670-labeled anti-miR-21 oligonucleotide payload. (A) Ex vivo fluorescence images of harvested organs after intravenous injection of saline as negative control (PBS column), control pSiNPs containing the nontargeting peptide CRA and loaded with a Quasar 670-labeled anti-miR-21 oligonucleotide (Control pSiNP column), and tumor-targeting CGKRK-pSiNPs loaded with a Quasar 670-labeled anti-miR-21 oligonucleotide (CGKRK pSiNP column). (B) Quantification of the fluorescence signal from the Quasar 670-labeled oligonucleotide payload in the harvested organs showing enhanced tumor accumulation of tumor-targeted CGKRK-pSiNPs relative to control nontargeted CRA-pSiNPs (mean value  $\pm$  SEM,  $n = 6$  per group,  $*p < 0.05$ ,  $**p < 0.01$ ,  $***p < 0.001$ ).

accumulation in the liver, heart, and kidneys (Figure 4B). This was consistent with the ability of the targeting CGKRK peptide to improve nanoparticle accumulation in the tumor. The results were confirmed by analysis of the FAM signal of the labeled peptides attached to the pSiNPs in the same harvested organs. The labeled peptide showed biodistribution profiles matching those observed for the labeled nucleic acid payload (Figure S6, SI), indicative of effective delivery of the intact nanoconstruct. This is also in accordance with the improved stability and circulation properties provided by the use of PEG as a nanoparticle coating.<sup>58,62–64</sup> Slower degradation and release kinetics were also expected *in vivo*, as it is known that a PEG shell grafted to the surface of pSiNPs delays the degradation of the silicon skeleton and that the formation of a protein corona around the nanoparticles forms a secondary barrier that influences the release profile of the payload.<sup>65,66</sup>

As mentioned above, the nontargeting control peptide CRA yielded somewhat greater accumulation in the heart and liver relative to the CGKRK-targeted particles. The greater accumulation seen in the liver is understandable given that the control peptide does not have strong affinity for the tumor and so it is expected to clear faster than the tumor-targeting CGKRK peptide. However, the reason for the greater accumulation of the CRA particles seen in the heart is not clear at this time. Although it can be difficult to use fluorescence imaging data to infer biodistribution in different organs due to differences in light absorbance and fluorophore quenching effects in the different tissues,<sup>67</sup> the greater

accumulation in heart seen for the CRA control particles is statistically significant, and both the peptide label and the anti-miR-21 label showed higher accumulation in this organ relative to the CGKRK particles. We note that the biodistribution analysis was based on the fluorescent signal of the nanoparticle nucleic acid payload and of the attached FAM-labeled peptide; therefore, additional portions of silicon material ending up in the liver during the course of the experiments may not have been detected. The *in vivo* therapeutic efficacy of the optimized anti-miR pSiNP formulation against a COV-318 xenograft tumor model was evaluated next. All the nanoparticle constructs used were stored in pure ethanol at 4 °C for at least 7 days prior to administration to mice. The particles were isolated from the ethanol solvent by centrifugation, resuspended in PBS, and used immediately. Mice were injected via the tail vein with a regimen consisting of five total doses (25 mg/kg), given on days 0, 1, 3, 5, and 7, which is in accordance with the administration protocol used for other anti-miR therapeutics.<sup>17,18,41,68</sup> Mice administered anti-miR-21 CGKRK-pSiNPs showed complete inhibition of tumor growth, and the total tumor volume did not increase during the 10-day assessment (Figure 5). In contrast, control tumor-bearing mice administered either PBS or CGKRK-pSiNPs loaded with a scrambled LNA sequence showed a 10-fold increase in tumor volume over the same time frame (Figure 5B), establishing that the therapeutic effect was associated with the anti-miR-21 LNA and its specific silencing action. Measurements of the mass of tumors collected from mice 10 days after the first injection of the formulations (Figure S7, SI) were consistent with the tumor volume measurements. Injection of a control formulation containing the competent anti-miR-21 LNA but delivered using the nontargeting CRA-pSiNP vehicle induced some reduction in tumor growth, but with significantly ( $p < 0.01$ ) less potency than anti-miR-21 CGKRK-pSiNPs. This result is consistent with the greater ability of the targeted CGKRK particles to home to tumor cells observed above (Figure 4), and it is consistent with the recent literature; in an article surveying the literature from the past 10 years, Wilhelm et al. noted that nanoparticle-based delivery is generally more efficient with inorganic nanoparticles that possess  $\zeta$ -potential values close to neutral and that employ active tumor targeting.<sup>69</sup>

To validate the connection between miR-21 silencing and inhibition of tumor growth, we quantified the knockdown of the target miR-21 in the tumor tissues by RT-qPCR. Tumors from mice that received anti-miR-21 CGKRK-pSiNPs displayed reduced miR-21 levels compared to those harvested from mice injected with scrambled LNA CGKRK-pSiNPs, and the potency observed was comparable to that obtained in the cell culture experiments. These results confirmed the effective silencing of miR-21 in the tumor (Figure 5C). The treatments appeared to be well-tolerated by the animals; the mean body weight of the mice gradually increased during the course of all treatments, with no substantial differences between any of the cohorts and no sudden drop in weight that might be indicative of the acute toxicity of the anti-miR formulations (Figure 5D).

## CONCLUSIONS

In conclusion, biodegradable porous silicon nanoparticles engineered to deliver tumor-targeted anti-miR therapeutics showed substantial anticancer activity in a xenograft model of ovarian cancer in mice by effectively silencing miR-21. To our

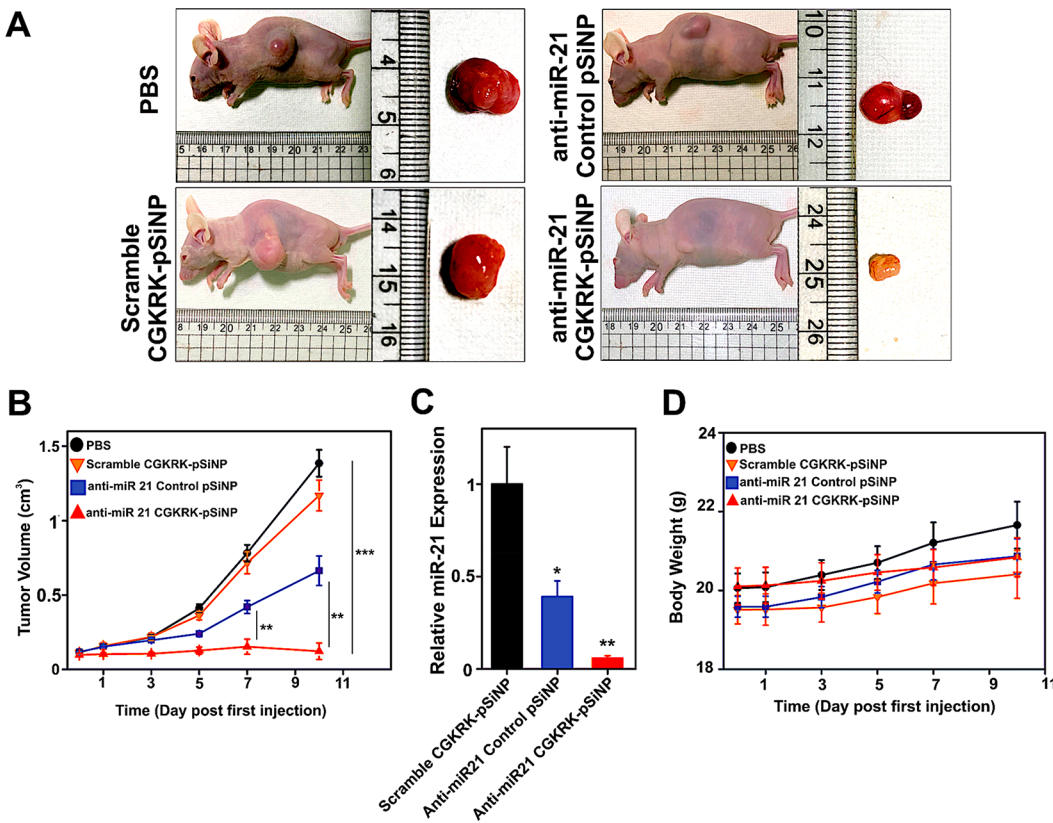


**Figure 5.** Anticancer activity in nude mice bearing subcutaneous COV-318 xenograft tumors. (A) Representative images of mice from groups administered the indicated treatments 10 days following the first injection and showing the harvested tumors. (B) Tumor growth curves after intravenous injection of the different nanoparticle formulations (a total of five injections over 7 days, beginning at day 0) (mean value  $\pm$  SEM,  $n = 6\text{--}7$  per group,  $**p < 0.01$ ,  $***p < 0.001$ ). (C) RT-qPCR of miR-21 extracted from the tumors of mice 10 days into the treatment regimen with the indicated nanoparticle formulations (mean value  $\pm$  SEM,  $n = 6\text{--}7$  per group, averaged for three technical replicates,  $*p < 0.05$ ,  $**p < 0.01$ ). (D) Body weight variation of the tumor-bearing mice over the course of the treatment with the indicated nanoparticle formulations (mean value  $\pm$  SEM,  $n = 6\text{--}7$  per group). No mice were excluded from the analysis.

knowledge, this is the first report of effective *in vivo* treatment of ovarian cancer leveraging an anti-miR-21 therapeutic agent. Looking forward, more complex models of ovarian cancer, including patient-derived orthotopic tumors or genetically engineered mouse models (GEMs), may be employed to further assess the efficacy of the therapeutic agents in tumor environments to improve the potential for clinical translation. The work also represents the first example of delivery of an LNA-based payload against a target microRNA with porous silicon nanoparticles, and it is notable for the substantial tumor targeting and tumor growth inhibition that could be achieved in mice. The calcium silicate-trapping chemistry enabled efficient loading of anti-miR-21 LNA oligonucleotides in the porous structure of the nanoparticles (17% by mass), which is difficult to achieve with many other nanoparticle systems. Another enabling element of the approach was the CGKRK targeting peptide, which binds to receptors overexpressed on the surface of tumor endothelial cells and therefore allowed internalization of the payload more specifically into the tumor cells. Therefore, this work demonstrates the modular nature of the pSiNP-based anti-miR therapeutic approach: the appropriate choice of the sequence of the nucleic acid payload and of the peptide ligand allows selective targeting of desired tissues for a more effective therapeutic outcome. The efficacy of the anti-miR approach demonstrated here for treatment of ovarian cancer suggests that porous silicon nanoparticles can serve as

an effective platform for delivery of microRNA-silencing therapeutics in other diseases.

## METHODS

**Preparation of Porous Silicon Nanoparticles.** The pSiNPs were prepared following the published “perforation etching” procedure.<sup>48</sup> Briefly, highly boron-doped  $p^{+}$ -type crystalline silicon wafers ( $\sim 1 \text{ m}\Omega \text{ cm}$  resistivity, 100 mm diameter, Virginia Semiconductor, Inc.) were electrochemically etched in an electrolyte consisting of 3:1 (v:v) 48% aqueous hydrofluoric acid (HF):ethanol. The etching waveform was composed of a square wave in which a lower current density of  $46 \text{ mA cm}^{-2}$  was applied for 1.818 s, followed by a higher current density pulse of  $365 \text{ mA cm}^{-2}$  applied for 0.363 s. Repetition of this waveform for 140 cycles generated stratified porous silicon films with thin, high-porosity “perforations” repeating approximately every 200 nm through the porous layer. This film was then removed from the silicon substrate (“lift off”) by application of a current density pulse of  $3.4 \text{ mA cm}^{-2}$  for 150 s in an electrolyte consisting of 1:20 (v:v) 48% aqueous HF:ethanol. The freestanding film was fragmented into nanoparticles by ultrasonication overnight in ethanol. The resulting pSiNPs, of average diameter  $182 \pm 6 \text{ nm}$  by dynamic light scattering (Z-average, intensity based, Zetasizer Zs90, Malvern Instruments), were dispersed in an aqueous solution of 0.8 mM sodium tetraborate for 1 h to grow a thin layer of silicon oxide on their surface. Following the reaction, oxidized pSiNPs were collected by centrifugation and stored in 100% ethanol.

**Characterization of Porous Silicon Nanoparticles.** The hydrodynamic diameter and  $\zeta$ -potential measurements were conducted on a Zetasizer Zs90 (Malvern Instruments). Size measure-

ments were carried out by dispersing the pSiNPs in deionized water, whereas  $\zeta$ -potential values were acquired by dispersion of pSiNPs in phosphate-buffered saline (PBS), pH 7.4. Transmission electron microscope (TEM) images were acquired with a JEOL-1200 EX II instrument. Attenuated total reflection Fourier transform infrared (ATR-FTIR) spectra were acquired using a Thermo Scientific Nicolet 6700 instrument fitted with a Smart iTR diamond ATR fixture. Porous layer porosity was measured using the spectroscopic liquid infiltration method (SLIM), a nondestructive optical interferometric technique described elsewhere.<sup>51</sup> Adsorption–desorption isotherms were acquired on dry particles at 77 K on an ASAP 2020 instrument (Micromeritics). Total pore volume was determined from adsorption–desorption isotherms, and pore size was determined using the Barrett–Joyner–Halenda (BJH) method. Infrared (IR) spectra were acquired as attenuated total reflectance Fourier-transform infrared spectra (ATR-FT-IR) from dry powder nanoparticle samples.

**Peptide Synthesis.** Peptides were synthesized using an automatic microwave-assisted peptide synthesizer (Liberty; CEM, Matthews, NC) using standard solid-phase chemistry. Peptides were synthesized with a 5-fluorescein carboxylate (FAM) label, a 6-aminohexanoic acid spacer (X) to separate the dye from the sequence, and a amide-blocked C-terminus. An extra cysteine with a free sulfhydryl group was added to the cyclic peptides for coupling purposes.<sup>70</sup> The tumor-targeting peptides used were iRGD (sequence CRGDKGPDC), iNGR (sequence CRNGRGPDC), CGKRK, and t-LyP-1 (sequence CGNKRTTR). The CRA and CREK peptides displayed little to no targeting efficacy and were used for control experiments. The *in vitro* experiments employed the CREK peptide (sequence CREK), whereas the CRA peptide (sequence CRA) was used for the *in vivo* experiments. The CRA peptide was purchased from Genscript (Piscataway, NJ).

**Preparation of LNA-Loaded Porous Silicon Nanoparticles.** Locked nucleic acid (LNA) oligonucleotides against miR-21 were synthesized and purified (HPLC purification) by Qiagen (Hilden, Germany). The anti-miR-21 oligonucleotide sequence was as follows: 5'-TCAACATCAGTCAGATAAGCTA-3', where LNA nucleotides are italic. A stock solution of 4 M calcium chloride ( $\text{CaCl}_2$ ) ( $M_w = 110.98$ , anhydrous, Spectrum Chemicals) was prepared in DNase-free water. For LNA loading, a dispersion of 0.25 mg of pSiNPs in 200  $\mu\text{L}$  of ethanol was mixed with 50  $\mu\text{L}$  of a 150  $\mu\text{M}$  LNA stock solution in DNase-free water, with 250  $\mu\text{L}$  of the 4 M  $\text{CaCl}_2$  solution. This gave a final concentration of 15  $\mu\text{M}$  LNA (7.5 nmol), 0.25 mg of pSiNPs, and 2 M  $\text{CaCl}_2$  in 0.5 mL of 1:1.5 ethanol:DNase-free water. The mixture was agitated for 60 min at room temperature and then centrifuged for 10 min. pSiNPs were washed once in DI water, once in 70% ethanol, and once in absolute ethanol. LNA loading was determined using a Quasar 570-labeled anti-miR-21 oligonucleotide and measuring the UV-vis absorption ( $\lambda = 548$  nm) of the supernatants from each centrifugation step using a UV-vis spectrophotometer (SpectraMax Plus 384, Molecular Devices). Using a calibration curve obtained from a standard solution of Quasar 570-labeled anti-miR-21 oligonucleotide at different concentrations, the loading was found to be 17% by mass, defined as the mass of LNA loaded divided by (mass of LNA loaded + mass of porous silicon)  $\times 100$ , which corresponded to 28 nmol LNA/mg of porous silicon. In parallel, the efficiency of the loading procedure was calculated and found to be  $97 \pm 2\%$ . The same procedure was applied when loading pSiNPs with a scrambled LNA sequence, 5'-CATTAATGTCGGACAACTCAAT-3', where the LNA oligonucleotides are italic. The same loading values were obtained for unlabeled LNA oligonucleotides as measured by means of a Nanodrop 2000 spectrophotometer (Thermo Scientific, ND-200). The release profile of the oligonucleotide payload from the calcium silicate-capped pSiNPs was obtained by dispersing 0.25 mg of pSiNPs loaded with Quasar 570-labeled anti-miR-21 oligonucleotide in 1 mL of PBS, pH 7.4, and incubating at 37 °C with mild shaking. The supernatant containing released labeled-oligonucleotides was collected at different time points (1, 2, 4, 10, 24 h) and analyzed by optical absorbance spectroscopy ( $\lambda = 548$  nm). Concentrations of the released

oligonucleotides were determined using a calibration curve obtained from a standard solution of the same labeled oligonucleotides.

**Conjugation of Tumor-Targeting Peptides to LNA-Loaded pSiNPs.** The above LNA-loaded pSiNPs (0.5 mg) were dispersed in 200  $\mu\text{L}$  of dichloromethane (DCM), and 50  $\mu\text{L}$  of a cyclic azasilane compound, 2,2-dimethoxy-1,6-diaza-2-silacyclooctane (DMDASCO), was added. The mixture was incubated under mild shaking, at room temperature, for 4 h and then centrifuged for 10 min. pSiNPs were washed once in DCM, and twice in ethanol. The aminated nanoparticles ( $\text{NH}_2\text{-LNA-pSiNPs}$ ) were then dispersed in ethanol (0.5 mg of nanoparticles in 80  $\mu\text{L}$  of ethanol), and a solution (180  $\mu\text{L}$ ) of the heterofunctional linker maleimide-PEG-succinimidyl valerate (MAL-PEG-SVA,  $M_w = 3400$ , Laysan Bio Inc.) in ethanol (5 mg/mL) was added. The mixture was incubated overnight, with mild shaking, at room temperature, and then centrifuged for 10 min to isolate the nanoparticles. The particles were then redispersed in ethanol and centrifuged (3 $\times$ ) to remove unbound PEG linkers. Peptide conjugation was then achieved by mixing a dispersion of the above PEGylated-pSiNPs (0.3 mg in 50  $\mu\text{L}$  ethanol) with an aliquot (50  $\mu\text{L}$ ) of a stock solution containing 0.6 mg/mL of peptide in DI water. The mixture was allowed to react at room temperature for 4 h, and then the particles were washed (dispersed, then separated by centrifuge) three times in ethanol and finally dispersed in pure ethanol. To avoid dissolution during storage, the final formulations were stored in pure ethanol at 4 °C, and they were isolated by centrifugation and resuspended in PBS solution immediately prior to administration. This procedure was carried out with no variations for all the peptides described in this study. The density of peptides grafted to the pSiNPs was determined using FAM-labeled peptides, by measurement of optical absorbance of the supernatant ( $\lambda = 548$  nm), and was found to be  $39 \pm 6$  nmol peptide/mg pSiNPs ( $n = 15$ ).

**Cell Culture.** The CAOV-3, COV-318, OVCAR-8, Kuramochi, KF-28, IGROV-1, and OWA42 cell lines were obtained from ATCC (Manassas, VA) and all were authenticated by STS testing at ATCC. Human OAW42 and COV-318 cells were grown in DMEM supplemented with 10% fetal bovine serum (FBS) and 1% penicillin/streptomycin (P/S) in a 5%  $\text{CO}_2$  humidified incubator at 37 °C. Human CAOV-3, OVCAR-8, KF-28, and IGROV-1 cells were cultured in RPMI-1640 supplemented with 10% FBS and 1% P/S in a 5%  $\text{CO}_2$  humidified incubator at 37 °C. Human Kuramochi cells were grown in RPMI-1640 supplemented with 10% FBS, 1% NEAA (non-essential amino acid), 4.0 mg/mL human insulin, and 1% P/S, in a 5%  $\text{CO}_2$  humidified incubator at 37 °C. Healthy human LP-9 cells were cultured in Medium 199 (modified with Earle's salts and glutamine) supplemented with 15% FBS and 0.4  $\mu\text{g}/\text{mL}$  hydrocortisone, in a 5%  $\text{CO}_2$  humidified incubator at 37 °C. Cells were passaged after reaching 80–90% confluence and detached using an enzyme-free dissociation buffer (Gibco, Thermo Fisher).

**Peptide-Functionalized Porous Silicon Nanoparticle Accumulation in Cultured Cells.** OAW42, COV-318, CAOV-3, OVCAR-8, KF-28, Kuramochi, IGROV-1, and LP-9 cells, approximately  $5 \times 10^4$  each, were seeded in 24-well culture plates, followed by addition of 0.5 mL of the relevant culture medium (see above), and grown overnight. Cell incubation with the different FAM-labeled peptide–pSiNP formulations was carried out with 0.025 mg/mL particle concentration in each well for 4 h in a 5%  $\text{CO}_2$  humidified incubator at 37 °C. Subsequently, the cells were harvested, washed three times with PBS, treated with 4% paraformaldehyde (PFA) in PBS (15 min, room temperature), and washed again three times with PBS. Cell samples were then analyzed by flow cytometry on a LSR Fortessa FACS analyzer (BD Biosciences). The peptides used were iRGD, iNGR, CGKRK, and t-LyP-1; “control” pSiNPs in these experiments used the CREK peptide. Sequences of all peptides are provided above (“Peptide Synthesis” section). The nanoparticles contained a DNA sequence mimicking the LNA payload, and they were sealed with the same calcium silicate capping and surface functionalization chemistries as used with the anti-miR-21 LNA containing samples.

**Confocal Microscopy.** OAW42 cells, approximately  $5 \times 10^4$ , were seeded on a square glass coverslip inside 6-well culture plates,

followed by addition of 2 mL of culture medium and incubation overnight. Cells were then cultured in the presence of 0.05 mg/mL FAM-labeled CGKRK-pSiNPs loaded with a Quasar 570-labeled anti-miR-21 oligonucleotide for 4 h. Cell samples were then split into two groups: one group was immediately fixed and worked up prior to confocal microscope analysis, the other one was cultured for an additional 24 h in fresh culture medium, after discarding the nanoparticle-containing medium, and then prepared for confocal microscopy analysis. Workup of the cell samples was as follows: the cell layer grown on the surface of the glass coverslip was (i) gently washed three times with PBS, (ii) fixed with 4% PFA in PBS (15 min, room temperature), (iii) washed three times with PBS, (iv) treated with DAPI for nucleus staining (10 min, room temperature, protected from light), and (v) washed three times with PBS. The coverslips were eventually mounted onto microscope glass slides. Confocal micrographs were acquired on a Zeiss LSM 710 NLO, using fluorescence excitation/emission filters for DAPI (cell nuclei), FAM (targeting peptide), and Cy3 (Quasar 570-labeled oligonucleotides).

**In Vitro RT-qPCR.** Quantitative reverse transcription polymerase chain reaction (RT-qPCR) was used to evaluate miR-21 expression and to investigate knockdown efficiency. OAW42 or COV-318 cells were incubated with free anti-miR-21 LNA (no carrier), anti-miR-21 CGKRK-pSiNPs, anti-miR-21 control CREK-pSiNPs, scrambled LNA CGKRK-pSiNPs, anti-miR-21 LNA loaded in a commercial Lipofectamine formulation (RNAi Max, Thermo Fisher) (positive control), and pure culture medium (negative control). “Anti-miR 21 control pSiNP” refers to pSiNPs loaded with the correct anti-miR-21 LNA but containing the nontargeting control peptide CREK. “Scramble CGKRK-pSiNP” is pSiNPs loaded with a scrambled anti-miR-21 sequence but containing the correct CGKRK targeting peptide sequence. Every formulation was dosed to give a total concentration of 100 nM LNA in the culture well. After 48 h incubation, cells were collected and total small RNA was extracted using the mirVana miRNA isolation kit following the manufacturer’s instructions (Thermo Fisher). To quantify miR-21 expression, a TaqMan microRNA assay was performed according to the manufacturer’s protocol (Thermo Fisher). Isolated RNA was first transcribed into cDNA following the manufacturer’s instructions (TaqMan microRNA reverse transcription kit, Thermo Fisher). Synthesized cDNA was subjected to qPCR (TaqMan universal master mix II, Thermo Fisher), and miR-21 expression was quantified via Taqman probe technology, using the specific primers and probe for miR-21 (hsa-miR-21, assay ID 00397, Thermo Fisher) and for U6 snRNA (U6 snRNA, assay ID 001973, Thermo Fisher) as an internal control. PCR amplification was conducted on a Stratagene Mx300SP qPCR system, and the data were analyzed using the comparative  $\Delta\Delta CT$  method.

**Caspase Assay.** OAW42 cells were seeded on 24-well culture plates, followed by addition of 0.5 mL of culture medium, and grown overnight. Cells were incubated with free anti-miR-21 LNA (no carrier), anti-miR-21 CGKRK-pSiNPs, anti-miR-21 control CREK-pSiNPs, scrambled LNA CGKRK-pSiNPs, 2  $\mu$ M camptothecin (positive control), and pure culture medium (negative control). Every formulation was dosed to give a total concentration of 100 nM LNA in the culture well. After 48 h incubation, cellular caspase-3 activity was examined using a caspase-3 fluorometric assay kit (Abcam) following the manufacturer’s instructions. Fluorescence intensity of the samples was measured on a Fluorolog-3 spectrophotometer (Horiba Scientific) using  $\lambda_{ex}/\lambda_{em}$  400/505 nm.

**Cell Viability Assay.** Cell viability was examined by means of the MTT assay. For model OAW42 cells, approximately  $8 \times 10^3$  cells were seeded on 96-well culture plates, followed by addition of 0.1 mL culture medium and incubation overnight. The cells were then incubated with free anti-miR-21 LNA (no carrier), anti-miR-21 CGKRK-pSiNPs, anti-miR-21 control CREK-pSiNPs, scrambled LNA CGKRK-pSiNPs, DMSO 30% (positive control), and pure culture medium (negative control). “Anti-miR 21 control pSiNP” refers to pSiNPs loaded with the correct anti-miR-21 LNA but containing the nontargeting control peptide CREK. “Scrambled LNA CGKRK-pSiNP” is pSiNPs loaded with a scrambled anti-miR-21

sequence but containing the correct CGKRK targeting peptide sequence. For each formulation, different doses were applied that respectively gave total concentrations of LNA in the culture well of 50, 100, or 200 nM. After 48 h of incubation, the MTT assay was performed following standard protocols, and the cell samples were eventually analyzed by optical absorbance spectroscopy ( $\lambda = 570$  nm) using a UV-vis plate reader (SpectraMax Plus 384, Molecular Devices). The MTT cell viability assay was performed on COV-318, CAOV-3, OVCAR-8, KF-28, Kuramochi, and IGROV-1 cells following the same procedure; cells were incubated with anti-miR-21 CGKRK-pSiNPs at a final LNA concentration of 200 nM.

**Animal Models.** All animal protocols were approved by the Institutional Animal Care and Use Committee (IACUC) of Kyung Hee University, Republic of Korea (Approval number: KHUASP (SE)-17-139). To generate subcutaneous tumor xenograft models, female nude mice (6 weeks) were subcutaneously inoculated in the right flank with  $2 \times 10^7$  COV-318 cells. Tumor size was monitored with a vernier caliper. When the tumor reached a volume of 50 mm<sup>3</sup>, the mice were weighed and randomized into groups for subsequent targeting and therapeutic studies.

**Biodistribution in Vivo.** To investigate pSiNP distribution in vivo, tumor-bearing mice were randomized into three groups (six mice per group) and intravenously injected (12.5 mg/kg) with (i) saline control, (ii) CGKRK-pSiNPs loaded with a Quasar 670-labeled anti-miR-21 oligonucleotide payload, or (iii) control CRA-pSiNPs loaded with a Quasar 670-labeled anti-miR-21 oligonucleotide payload. The mice were sacrificed 5 h postinjection and major internal organs, including the lung, heart, liver, spleen, and kidneys, in addition to the tumor were harvested and analyzed by fluorescence imaging with an IVIS 200 (Xenogen) using the Cy5.5 filter acquisition window.

**Therapeutic Efficacy in Vivo.** Tumor-bearing mice, when the tumor reached a volume of 50 mm<sup>3</sup>, were randomized into four groups (six or seven mice per group) and intravenously injected (tail vein, 25 mg/kg, corresponding to ~10 nmol of LNA per injection) with (i) saline control (seven mice), (ii) anti-miR-21 CGKRK-pSiNPs (seven mice), (iii) anti-miR-21 control CRA-pSiNPs (six mice), or (iv) scrambled LNA CGKRK-pSiNPs (seven mice). Tumor growth was evaluated by measuring the tumor volume over the course of five injections given at days 0, 1, 3, 5, and 7. The tumor volume was calculated as  $V = (lw^2)/2$ , where  $l$  is the length and  $w$  is the width of the tumor measured on the live animal using a vernier caliper. At the end of the relevant timeline (day 10), mice were sacrificed and tumors were collected for visualization and weight analysis. No mice were excluded from the analysis. “PBS” is a negative control of tumor mice injected with saline, “anti-miR-21 control pSiNP” is pSiNPs loaded with the correct anti-miR-21 LNA but containing the nontargeting control peptide CRA, “scrambled LNA CGKRK-pSiNP” is pSiNPs containing the correct CGKRK targeting peptide sequence but loaded with a scrambled anti-miR-21 sequence, and “anti-miR-21 CGKRK-pSiNP” is the candidate anticancer formulation. To quantify miR-21 knockdown associated with the treatment, RT-qPCR was performed on the tumor tissues collected from mice on day 10 of a regimen consisting of administration of the relevant anti-miR-21 CGKRK-pSiNPs, anti-miR-21 control CRA-pSiNPs, and scrambled LNA CGKRK-pSiNPs formulations. Total small RNA was extracted from flash-frozen tumor tissues using the mirVana isolation kit following the manufacturer’s instructions (Thermo Fisher). To quantify miR-21 expression, TaqMan microRNA assay was performed according to the manufacturer’s protocol (Thermo Fisher) and following the procedure described previously for in vitro RT-qPCR. PCR amplification was analyzed using the comparative  $\Delta\Delta CT$  method and normalized for tumor size.

**Statistical Analysis.** All experiments reported in this study are based on at least three independent replicates. Statistical analysis was conducted using two-tailed Student’s test for two mean values or analysis of variance (ANOVA) followed by the Bonferroni test for multiple values. SD indicates sample standard deviation, whereas SEM indicates standard error of the mean. Unless otherwise noted,  $p < 0.05$  was considered statistically significant.

## ASSOCIATED CONTENT

### Supporting Information

The Supporting Information is available free of charge on the ACS Publications website at DOI: [10.1021/acsmi.9b07980](https://doi.org/10.1021/acsmi.9b07980).

Dynamic light scattering (DLS) data on pSiNPs, in vitro nucleic acid release data, Fourier-transform infrared (FT-IR) spectra, additional confocal microscopy data on cellular uptake, flow cytometry data evaluating localization efficiency for different ovarian cancer cells, in vivo biodistribution data, and tumor mass data for treated and control animals ([PDF](#))

## AUTHOR INFORMATION

### Corresponding Authors

\*H.-J.J. e-mail: [hjiang@khu.ac.kr](mailto:hjiang@khu.ac.kr).

\*M.J.S. e-mail: [msailor@ucsd.edu](mailto:msailor@ucsd.edu).

### ORCID

Francesco Ricci: [0000-0003-4941-8646](#)

Michael J. Sailor: [0000-0002-4809-9826](#)

### Author Contributions

✉A.B. and K.-H.K contributed equally to this work.

### Notes

The authors declare the following competing financial interest(s): M.J.S. is a scientific founder of Spinnaker Biosciences, Inc., and has an equity interest in the company. Although this project has been identified for conflict of interest management on the basis of its overall scope and its potential benefit to Spinnaker Biosciences, Inc., the research findings included in this particular publication may not necessarily relate to the interests of Spinnaker Biosciences, Inc. The terms of this arrangement have been reviewed and approved by the University of California, San Diego, in accordance with its conflict of interest policies.

## ACKNOWLEDGMENTS

We thank Venkata Ramana Kotamraju for the peptide synthesis. This work was supported in part by the National Institutes of Health grants R01CA214550-01 and R24 EY022025-01 and by the National Science Foundation grant CBET-1603177. This project received funding from the European Union's Horizon 2020 research and innovation program under the Marie Skłodowska-Curie grant agreement No 704120 ("MIRNANO") and from the Basic Science Research Program through the National Research Foundation of Korea (Ministry of Education, Science and Technology, NRF-2017R1A2B4003422). D.K. acknowledges the financial support received by the Bio & Medical Technology Development Program of the National Research Foundation (NRF), funded by the Ministry of Science & ICT (NRF-2018M3A9H3021707). A.B. is a Global Marie Skłodowska-Curie Fellow.

## REFERENCES

- (1) Siegel, R. L.; Miller, K. D.; Jemal, A. Cancer Statistics, 2018. *CA Cancer J. Clin.* **2018**, *68*, 7–30.
- (2) Jayson, G. C.; Kohn, E. C.; Kitchener, H. C.; Ledermann, J. A. Ovarian Cancer. *Lancet* **2014**, *384*, 1376–1388.
- (3) Matsuo, K.; Lin, Y. G.; Roman, L. D.; Sood, A. K. Overcoming Platinum Resistance in Ovarian Carcinoma. *Expert Opin. Invest. Drugs* **2010**, *19*, 1339–1354.
- (4) Iorio, M. V.; Visone, R.; Di Leva, G.; Donati, V.; Petrocca, F.; Casalini, P.; Taccioli, C.; Volinia, S.; Liu, C. G.; Alder, H.; Calin, G. A.; Ménard, S.; Croce, C. M. MicroRNA Signatures in Human Ovarian Cancer. *Cancer Res.* **2007**, *67*, 8699–8707.
- (5) Zaman, M. S.; Maher, D. M.; Khan, S.; Jaggi, M.; Chauhan, S. C. Current Status and Implications of MicroRNAs in Ovarian Cancer Diagnosis and Therapy. *J. Ovarian Res.* **2012**, *5*, 44.
- (6) van Jaarsveld, M. T. M.; Helleman, H.; Berns, E. M.; Wiemer, E. A. MicroRNAs in Ovarian Cancer Biology and Therapy Resistance. *Int. J. Biochem. Cell Biol.* **2010**, *42*, 1282–1290.
- (7) He, L.; Hannon, G. J. MicroRNAs: Small RNAs with a Big Role in Gene Regulation. *Nat. Rev. Genet.* **2004**, *5*, 522–531.
- (8) Esquela-Kerscher, A.; Slack, F. J. Oncomirs - MicroRNAs with a Role in Cancer. *Nat. Rev. Cancer* **2006**, *6*, 259–269.
- (9) Iorio, M. V.; Croce, C. M. MicroRNA Dysregulation in Cancer: Diagnostics, Monitoring and Therapeutics. A Comprehensive Review. *EMBO Mol. Med.* **2012**, *4*, 143–159.
- (10) Kong, Y. W.; Ferland-McCollough, D.; Jackson, T. J.; Bushell, M. MicroRNAs in Cancer Management. *Lancet Oncol.* **2012**, *13*, e249–e258.
- (11) Sethi, S.; Ali, S.; Sethi, S.; Sarkar, F. H. MicroRNAs in Personalized Cancer Therapy. *Clin. Genet.* **2014**, *86*, 68–73.
- (12) Li, Z.; Rana, T. M. Therapeutic Targeting of MicroRNAs: Current Status and Future Challenges. *Nat. Rev. Drug Discovery* **2014**, *13*, 622–638.
- (13) Rupaimole, R.; Slack, F. J. MicroRNA Therapeutics: Towards a New Era for the Management of Cancer and Other Diseases. *Nat. Rev. Drug Discovery* **2017**, *16*, 203–222.
- (14) Lewis, B. P.; Burge, C. B.; Bartel, D. P. Conserved Seed Pairing, Often Flanked by Adenosines, Indicates that Thousands of Human Genes are MicroRNA Targets. *Cell* **2005**, *120*, 15–20.
- (15) Cheng, C. J.; Bahal, R.; Babar, I. A.; Pincus, Z.; Barrera, F.; Liu, C.; Svoronos, A.; Braddock, D. T.; Glazer, P. M.; Engelmann, D. M.; Saltzman, W. M.; Slack, F. J. MicroRNA Silencing for Cancer Therapy Targeted to the Tumour Microenvironment. *Nature* **2015**, *518*, 107–110.
- (16) Devulapally, R.; Sekar, N. M.; Sekar, T. V.; Foygel, K.; Massoud, T. F.; Willmann, J. K.; Paulmurgan, R. Polymer Nanoparticles Mediated Codelivery of AntimiR-10b and AntimiR-21 for Achieving Triple Negative Breast Cancer Therapy. *ACS Nano* **2015**, *9*, 2290–2302.
- (17) Xu, X.; Ayub, B.; Liu, Z.; Serna, V. A.; Qiang, W.; Liu, Y.; Hernando, E.; Zabludoff, S.; Kurita, T.; Kong, B.; Wei, J. J. Anti-miR182 Reduces Ovarian Cancer Burden, Invasion, and Metastasis: an *in vivo* Study in Orthotopic Xenografts of Nude Mice. *Mol. Cancer Ther.* **2014**, *13*, 1729–1739.
- (18) Obad, S.; dos Santos, C. O.; Petri, A.; Heidenblad, M.; Broom, O.; Ruse, C.; Fu, C.; Lindow, M.; Stenvang, J.; Straarup, E. M.; Hansen, H. F.; Koch, T.; Pappin, D.; Hannon, G. J.; Kauppinen, S. Silencing of MicroRNA Families by Seed-Targeting Tiny LNAs. *Nat. Genet.* **2011**, *43*, 371–378.
- (19) Fabbri, E.; Brognara, E.; Borgatti, M.; Lampronti, I.; Finotti, A.; Bianchi, N.; Sforza, S.; Tedeschi, T.; Manicardi, A.; Marchelli, R.; Corradini, R.; Gambari, R. MiRNA Therapeutics: Delivery and Biological Activity of Peptide Nucleic Acids Targeting MiRNAs. *Epinigenomics* **2011**, *3*, 733–745.
- (20) Ganju, A.; Khan, S.; Hafeez, B. B.; Behrman, S. W.; Yallapu, M. M.; Chauhan, S. C.; Jaggi, M. MiRNA Nanotherapeutics for Cancer. *Drug Discovery Today* **2017**, *22*, 424–432.
- (21) Chen, Y.; Zhu, X.; Zhang, X.; Liu, B.; Huang, L. Nanoparticles Modified with Tumor-targeting scFv Deliver SiRNA and MiRNA for Cancer Therapy. *Mol. Ther.* **2010**, *18*, 1650–1656.
- (22) Shi, S. J.; Zhong, Z. R.; Liu, J.; Zhang, Z. R.; Sun, X.; Gong, T. Solid Lipid Nanoparticles Loaded with Anti-microRNA Oligonucleotides (AMOs) for Suppression of MicroRNA-21 Functions in Human Lung Cancer Cells. *Pharm. Res.* **2012**, *29*, 97–109.
- (23) Hatakeyama, H.; Murata, M.; Sato, Y.; Takahashi, M.; Minakawa, N.; Matsuda, A.; Harashima, H. The Systemic Administration of an Anti-miRNA Oligonucleotide Encapsulated pH-sensitive Liposome Results in Reduced Level of Hepatic MicroRNA-122 in Mice. *J. Controlled Release* **2014**, *173*, 43–50.

- (24) Babar, I. A.; Cheng, C. J.; Booth, C. J.; Liang, X.; Weidhaas, J. B.; Saltzman, W. M.; Slack, F. J. Nanoparticle-based Therapy in an *in vivo* MicroRNA-155 (miR-155)-dependent Mouse Model of Lymphoma. *Proc. Natl. Acad. Sci. U. S. A.* **2012**, *109*, E1695–E1704.
- (25) Cheng, C. J.; Saltzman, W. M. Polymer Nanoparticle-mediated Delivery of MicroRNA Inhibition and Alternative Splicing. *Mol. Pharmaceutics* **2012**, *9*, 1481–1488.
- (26) Conde, J.; Rosa, J.; de la Fuente, J. M.; Baptista, P. V. Gold-nanobeacons for Simultaneous Gene Specific Silencing and Intracellular Tracking of the Silencing Events. *Biomaterials* **2013**, *34*, 2516–2523.
- (27) Ren, Y.; Wang, R.; Gao, L.; Li, K.; Zhou, X.; Guo, H.; Liu, C.; Han, D.; Tian, J.; Ye, Q.; Hu, Y. T.; Sun, D.; Yuan, X.; Zhang, N. Sequential Co-delivery of MiR-21 Inhibitor Followed by Burst Release Doxorubicin Using NIR-responsive Hollow Gold Nanoparticle to Enhance Anticancer Efficacy. *J. Controlled Release* **2016**, *228*, 74–86.
- (28) Zhang, P.; Cheng, F.; Zhou, R.; Cao, J.; Li, J.; Burda, C.; Min, Q.; Zhu, J. J. DNA-Hybrid-gated Multifunctional Mesoporous Silica Nanocarriers for Dual-targeted and MicroRNA-responsive Controlled Drug Delivery. *Angew. Chem., Int. Ed.* **2014**, *53*, 2371–2375.
- (29) Bertucci, A.; Prasetyanto, E. A.; Septiadi, D.; Manicardi, A.; Brognara, E.; Gambari, R.; Corradini, R.; De Cola, L. Combined Delivery of Temozolomide and Anti-miR221 PNA Using Mesoporous Silica Nanoparticles Induces Apoptosis in Resistant Glioma Cells. *Small* **2015**, *11*, 5687–5695.
- (30) Yu, C.; Qian, L.; Ge, J.; Fu, J.; Yuan, P.; Yao, S. C. L.; Yao, S. Q. Cell-Penetrating Poly (disulfide) Assisted Intracellular Delivery of Mesoporous Silica Nanoparticles for Inhibition of MiR-21 Function and Detection of Subsequent Therapeutic Effects. *Angew. Chem., Int. Ed.* **2016**, *55*, 9272–9276.
- (31) Li, W.; Liu, Z.; Fontana, F.; Ding, Y.; Liu, D.; Hirvonen, J. T.; Santos, H. A. Tailoring Porous Silicon for Biomedical Applications: From Drug Delivery to Cancer Immunotherapy. *Adv. Mater.* **2018**, *30*, 1703740.
- (32) Kwon, E. J.; Skalak, M.; Bertucci, A.; Braun, G.; Ricci, F.; Ruoslahti, E.; Sailor, M. J.; Bhatia, S. N. Porous Silicon Nanoparticle Delivery of Tandem Peptide Anti-Infectives for the Treatment of *Pseudomonas aeruginosa* Lung Infections. *Adv. Mater.* **2017**, *29*, 1701527.
- (33) Prestidge, C. A.; Barnes, T. J.; Lau, C. H.; Barnett, C.; Loni, A.; Canham, L. Mesoporous Silicon: a Platform for the Delivery of Therapeutics. *Expert Opin. Drug Delivery* **2007**, *4*, 101–110.
- (34) (a) Park, J. H.; Gu, L.; Von Maltzahn, G.; Ruoslahti, E.; Bhatia, S. N.; Sailor, M. J. Biodegradable Luminescent Porous Silicon Nanoparticles for *in vivo* Applications. *Nat. Mater.* **2009**, *8*, 331–336. (b) Kang, J.; Joo, J.; Kwon, E. J.; Skalak, M.; Hussain, S.; She, Z. G.; Ruoslahti, E.; Bhatia, S. N.; Sailor, M. J. Self-sealing Porous Silicon-calcium Silicate Core–shell Nanoparticles for Targeted siRNA Delivery to the Injured Brain. *Adv. Mater.* **2016**, *28*, 7962–7969. (c) Chiappini, C.; De Rosa, E.; Martinez, J. O.; Liu, X.; Steele, J.; Stevens, M. M.; Tasciotti, E. Biodegradable Silicon Nanoneedles Delivering Nucleic Acids Intracellularly Induce Localized *in vivo* Neovascularization. *Nat. Mater.* **2015**, *14*, 532–539. (d) Shen, J.; Xu, R.; Mai, J.; Kim, H. C.; Guo, X.; Qin, G.; Yang, Y.; Wolfram, J.; Mu, C.; Xia, X.; Gu, J.; Liu, X.; Mao, Z. W.; Ferrari, M.; Shen, H. High Capacity Nanoporous Silicon Carrier for Systemic Delivery of Gene Silencing Therapeutics. *ACS Nano* **2013**, *7*, 9867–9880.
- (35) (a) Wan, Y.; Apostolou, S.; Dronov, R.; Kuss, B.; Voelcker, N. H. Cancer-targeting SiRNA Delivery from Porous Silicon Nanoparticles. *Nanomedicine* **2014**, *9*, 2309–2321. (b) Hasanzadeh Kafshgari, M. H.; Alnakhli, M.; Delalat, B.; Apostolou, S.; Harding, F. J.; Mäkilä, E.; Salonen, J. J.; Kuss, B. J.; Voelcker, N. H. Small Interfering RNA Delivery by Polyethylenimine-functionalised Porous Silicon Nanoparticles. *Biomater. Sci.* **2015**, *3*, 1555–1565. (c) Zhang, M.; Xu, R.; Xia, X.; Yang, Y.; Gu, J.; Liu, G. X.; Ferrari, M.; Shen, H.; Qin, G. Polycation-functionalized Nanoporous Silicon Particles for Gene Silencing on Breast Cancer Cells. *Biomaterials* **2014**, *35*, 423–431.
- (36) Beavers, K. R.; Werfel, T. A.; Shen, T.; Kavanaugh, T. E.; Kilchrist, K. V.; Mares, J. W.M.; Fain, J. S.; Wiese, C. B.; Vickers, K. C.; Weiss, S. M.; Duvall, C. L. Porous Silicon and Polymer Nanocomposites for Delivery of Peptide Nucleic Acids as Anti-MicroRNA Therapies. *Adv. Mater.* **2016**, *28*, 7984–7992.
- (37) Si, M. L.; Zhu, S.; Wu, H.; Lu, Z.; Wu, F.; Mo, Y. Y. MiR-21-mediated Tumor Growth. *Oncogene* **2007**, *26*, 2799–2803.
- (38) Medina, P. P.; Nolde, M.; Slack, F. J. OncomiR Addiction in an *in vivo* Model of MicroRNA-21-induced pre-B-cell Lymphoma. *Nature* **2010**, *467*, 86–90.
- (39) Pan, X.; Wang, Z. X.; Wang, R. MicroRNA-21: a Novel Therapeutic Target in Human Cancer. *Cancer Biol. Ther.* **2010**, *10*, 1224–1232.
- (40) Sicard, F.; Gayral, M.; Lulka, H.; Buscail, L.; Cordelier, P. Targeting MiR-21 for the Therapy of Pancreatic Cancer. *Mol. Ther.* **2013**, *21*, 986–994.
- (41) Lee, T. J.; Yoo, J. Y.; Shu, D.; Li, H.; Zhang, J.; Yu, J. G.; Jaime-Ramirez, A. C.; Acunzo, M.; Romano, G.; Cui, R.; Sun, H. L.; et al. RNA Nanoparticle-based Targeted Therapy for Glioblastoma through Inhibition of Oncogenic MiR-21. *Mol. Ther.* **2017**, *25*, 1544–1555.
- (42) Yung, B. C.; Li, J.; Zhang, M.; Cheng, X.; Li, H.; Yung, E. M.; Kang, C.; Cosby, L. E.; Liu, Y.; Teng, L.; Lee, R. J. Lipid Nanoparticles Composed of Quaternary Amine–Tertiary Amine Cationic Lipid Combination (QTsome) for Therapeutic Delivery of AntimiR-21 for Lung Cancer. *Mol. Pharmaceutics* **2016**, *13*, 653–662.
- (43) Lou, Y.; Yang, X.; Wang, F.; Cui, Z.; Huang, Y. MicroRNA-21 Promotes the Cell Proliferation, Invasion and Migration Abilities in Ovarian Epithelial Carcinomas through Inhibiting the Expression of PTEN Protein. *Int. J. Mol. Med.* **2010**, *26*, 819–827.
- (44) Chan, J. K.; Blansit, K.; Kiet, T.; Sherman, A.; Wong, G.; Earle, C.; Bourguignon, L. Y. The Inhibition of MiR-21 Promotes Apoptosis and Chemosensitivity in Ovarian Cancer. *Gynecol. Oncol.* **2014**, *132*, 739–744.
- (45) Nedaeinia, R.; Sharifi, M.; Avan, A.; Kazemi, M.; Rafiee, L.; Ghayour-Mobarhan, M.; Salehi, R. Locked Nucleic Acid Anti-miR-21 Inhibits Cell Growth and Invasive Behaviors of a Colorectal Adenocarcinoma Cell Line: LNA-anti-miR as a Novel Approach. *Cancer Gene Ther.* **2016**, *23*, 246–253.
- (46) Veedu, R. N.; Wengel, J. Locked Nucleic Acids: Promising Nucleic Acid Analogs for Therapeutic Applications. *Chem. Biodiversity* **2010**, *7*, 536–542.
- (47) Chakraborty, C.; Sharma, A. R.; Sharma, G.; Doss, C. G. P.; Lee, S. S. Therapeutic MiRNA and SiRNA: Moving from Bench to Clinic as Next Generation Medicine. *Mol. Ther.–Nucleic Acids* **2017**, *8*, 132–143.
- (48) Qin, Z.; Joo, J.; Gu, L.; Sailor, M. J. Size Control of Porous Silicon Nanoparticles by Electrochemical Perforation Etching. *Part. Part. Syst. Charact.* **2014**, *31*, 252–256.
- (49) Segal, E.; Perelman, L. A.; Cunin, F.; Di Renzo, F.; Devoisselle, J. M.; Li, Y. Y.; Sailor, M. J. Confinement of Thermoresponsive Hydrogels in Nanostructured Porous Silicon Dioxide Templates. *Adv. Funct. Mater.* **2007**, *17*, 1153–1162.
- (50) Kim, D.; Zuidema, J. M.; Kang, J.; Pan, Y.; Wu, L.; Warther, D.; Arkles, B.; Sailor, M. J. Facile Surface Modification of Hydroxylated Silicon Nanostructures Using Heterocyclic Silanes. *J. Am. Chem. Soc.* **2016**, *138*, 15106–15109.
- (51) Ruoslahti, E. Peptides as Targeting Elements and Tissue Penetration Devices for Nanoparticles. *Adv. Mater.* **2012**, *24*, 3747–3756.
- (52) Ruoslahti, E.; Bhatia, S. N.; Sailor, M. J. Targeting of Drugs and Nanoparticles to Tumors. *J. Cell Biol.* **2010**, *188*, 759–768.
- (53) Kim, D.; Kang, J.; Wang, T.; Ryu, H. G.; Zuidema, J. M.; Joo, J.; Kim, M.; Huh, Y.; Jung, J.; Ahn, K. H.; Kim, K. H.; Sailor, M. J. Two photon *in vivo* Imaging with Porous Silicon Nanoparticles. *Adv. Mater.* **2017**, *29*, 1703309.
- (54) Mann, A. P.; Scodeller, P.; Hussain, S.; Joo, J.; Kwon, E. J.; Braun, G. B.; Mölder, T.; She, Z. G.; Kotamraju, V. R.; Ranscht, B.; Krajewski, S.; Teesalu, T.; Bhatia, S. N.; Sailor, M. J.; Ruoslahti, E. A

- Peptide for Targeted, Systemic Delivery of Imaging and Therapeutic Compounds into Acute Brain Injuries. *Nat. Commun.* **2016**, *7*, 11980.
- (55) Wang, C. F.; Sarparanta, M. P.; Mäkilä, E. M.; Hyvönen, M. L.; Laakkonen, P. M.; Salonen, J. J.; Hirvonen, J. T.; Airaksinen, A. J.; Santos, H. A. Multifunctional Porous Silicon Nanoparticles for Cancer Theranostics. *Biomaterials* **2015**, *48*, 108–118.
- (56) Kinnari, P. J.; Hyvönen, M. L.; Mäkilä, E. M.; Kaasalainen, M. H.; Rivinoja, A.; Salonen, J. J.; Hirvonen, J. T.; Laakkonen, P. M.; Santos, H. A. Tumour Homing Peptide-functionalized Porous Silicon Nanovectors for Cancer Therapy. *Biomaterials* **2013**, *34*, 9134–9141.
- (57) (a) Sugahara, K. N.; Teesalu, T.; Karmali, P. P.; Kotamraju, V. R.; Agemy, L.; Girard, O. M.; Hanahan, D.; Mattrey, R. F.; Ruoslahti, E. Tissue-penetrating Delivery of Compounds and Nanoparticles into Tumors. *Cancer Cell* **2009**, *16*, 510–520. (b) Alberici, L.; Roth, L.; Sugahara, K. N.; Agemy, L.; Kotamraju, V. R.; Teesalu, T.; Bordignon, C.; Traversari, C.; Rizzardi, G. P.; Ruoslahti, E. De novo Design of a Tumor-penetrating Peptide. *Cancer Res.* **2013**, *73*, 804–812. (c) Hoffman, J. A.; Giraudo, E.; Singh, M.; Zhang, L.; Inoue, M.; Porkka, K.; Hanahan, D.; Ruoslahti, E. Progressive Vascular Changes in a Transgenic Mouse Model of Squamous Cell Carcinoma. *Cancer Cell* **2003**, *4*, 383–391. (d) Roth, L.; Agemy, L.; Kotamraju, V. R.; Braun, G.; Teesalu, T.; Sugahara, K. N.; Hamzah, J.; Ruoslahti, E. Transtumoral Targeting Enabled by a Novel Neuropilin-binding Peptide. *Oncogene* **2012**, *31*, 3754–3763.
- (58) Zanuy, D.; Sayago, F. J.; Revilla-Lopez, G.; Ballano, G.; Agemy, L.; Kotamraju, V. R.; Jiménez, A. I.; Cativiela, C.; Nussinov, R.; Sawvel, A. M.; Stucky, G.; Ruoslahti, E.; Alemán, C. Engineering Strategy to Improve Peptide Analogs: from Structure-based Computational Design to Tumor Homing. *J. Comput. Aided Mol. Des.* **2013**, *27*, 31–43.
- (59) Kyle, A. H.; Baker, J. H. E.; Gandolfo, M. J.; Reinsberg, S. A.; Minchinton, A. I. Tissue Penetration and Activity of Camptothecins in Solid Tumor Xenografts. *Mol. Cancer Ther.* **2014**, *13*, 2727–2737.
- (60) Agemy, L.; Kotamraju, V. R.; Friedmann-Morvinski, D.; Sharma, S.; Sugahara, K. N.; Ruoslahti, E. Proapoptotic Peptide-mediated Cancer Therapy Targeted to Cell Surface p32. *Mol. Ther.* **2013**, *21*, 2195–2204.
- (61) (a) Fogal, V.; Zhang, L.; Krajewski, S.; Ruoslahti, E. Mitochondrial/Cell-surface Protein p32/gC1qR as a Molecular Target in Tumor Cells and Tumor Stroma. *Cancer Res.* **2008**, *68*, 7210–7218. (b) Ren, Y.; Cheung, H. W.; von Maltzhan, G.; Agrawal, A.; Cowley, G. S.; Weir, B. A.; Boehm, J. S.; Tamayo, P.; Karst, A. M.; Liu, J. F.; Hirsch, M. S.; Mesirov, J. P.; Drapkin, R.; Root, D. E.; Lo, J.; Fogal, V.; Ruoslahti, E.; Hahn, W. C.; Bhatia, S. N. Targeted Tumor-penetrating SiRNA Nanocomplexes for Credentialing the Ovarian Cancer Oncogene ID4. *Sci. Transl. Med.* **2012**, *4*, 147ra112. (c) Yu, G.; Wang, J. Significance of Hyaluronan Binding Protein (HABP1/p32/gC1qR) Expression in Advanced Serous Ovarian Cancer Patients. *Exp. Mol. Pathol.* **2013**, *94*, 210–215.
- (62) Nääkki, S.; Rytkönen, J.; Nissinen, T.; Florea, C.; Riikonen, J.; Ek, P.; Zhang, H.; Santos, H. A.; Närvänen, A.; Xu, W.; Lehto, V. P. Improved Stability and Biocompatibility of Nanostructured Silicon Drug Carrier for Intravenous Administration. *Acta Biomater.* **2015**, *13*, 207–215.
- (63) Gu, L.; Hall, D. J.; Qin, Z.; Anglin, E.; Joo, J.; Mooney, D. J.; Howell, S. B.; Sailor, M. J. *In vivo* Time-gated Fluorescence Imaging with Biodegradable Luminescent Porous Silicon Nanoparticles. *Nat. Commun.* **2013**, *4*, 2326.
- (64) Fang, C.; Shi, B.; Pei, Y. Y.; Hong, M. H.; Wu, J.; Chen, H. Z. *In vivo* Tumor Targeting of Tumor Necrosis Factor- $\alpha$ -loaded Stealth Nanoparticles: Effect of MePEG Molecular Weight and Particle Size. *Eur. J. Pharm. Sci.* **2006**, *27*, 27–36.
- (65) Godin, B.; Gu, J.; Serda, R. E.; Bhavane, R.; Tasciotti, E.; Chiappini, C.; Liu, X.; Tanaka, T.; Decuzzi, P.; Ferrari, M. Tailoring the Degradation Kinetics of Mesoporous Silicon Structures Through PEGylation. *J. Biomed. Mater. Res., Part A* **2010**, *94A*, 1236–1243.
- (66) Behzadi, S.; Serpooshan, V.; Sakhtianchi, R.; Müller, B.; Landfester, K.; Crespy, D.; Mahmoudi, M. Protein Corona Change the Drug Release Profile of Nanocarriers: the “Overlooked” Factor at the Nanobio Interface. *Colloids Surf, B* **2014**, *123*, 143–149.
- (67) Meng, F.; Wang, J.; Ping, Q.; Yeo, Y. Quantitative Assessment of Nanoparticle Biodistribution by Fluorescence Imaging, Revisited. *ACS Nano* **2018**, *12*, 6458–6468.
- (68) Huynh, C.; Segura, M. F.; Gaziel-Sovran, A.; Menendez, S.; Darvishian, F.; Chiriboga, L.; Levin, B.; Meruelo, D.; Osman, I.; Zavadil, J.; Marcusson, E. G.; Hernando, E. Efficient *in vivo* MicroRNA Targeting of Liver Metastasis. *Oncogene* **2011**, *30*, 1481–1488.
- (69) Wilhelm, S.; Tavares, A. J.; Dai, Q.; Ohta, S.; Audet, J.; Dvorak, H. F.; Chan, W. C. Analysis of Nanoparticle Delivery to Tumours. *Nat. Rev. Mater.* **2016**, *1*, 16014.
- (70) Teesalu, T.; Sugahara, K. N.; Kotamraju, V. R.; Ruoslahti, E. C-end Rule Peptides Mediate Neuropilin-1-dependent Cell, Vascular, and Tissue penetration. *Proc. Natl. Acad. Sci. U. S. A.* **2009**, *106*, 16157–16162.